JOURNAL OF SPACECRAFT AND ROCKETS
Vol. 48, No. 4, July–August 2011

Boundary-Layer Transition on a Hypersonic Forebody: Experiments and Calculations

Evgeniy Orlik,* Ivan Fedioun,† and Dmitry Davidenko‡
Centre National de la Recherche Scientifique, 45071 Orléans Cedex 2, France

DOI: 10.2514/1.51570

The natural laminar–turbulent transition of the flow under a hypersonic forebody is investigated, both experimentally and numerically. Experiments are conducted on a 1:3-scale model, in the T-313 conventional blowdown wind tunnel of the Institute of Theoretical and Applied Mechanics–Russian Academy of Science at Novosibirsk, at Mach numbers 4 and 6. The transition is detected from pitot pressure measurements in the boundary layer. Transition onset occurs very near the nose at Mach 4 and is delayed to the middle part of the forebody at Mach 6. For the stability analysis, the mean flow is obtained from Navier–Stokes calculations for the wind-tunnel conditions. The local modal linear stability theory, coupled with the e^N method, is applied in a three-dimensional fully compressible formulation. At Mach 4, transition is due to a traveling crossflow instability, and a weak oblique first mode coexists independently. At Mach 6, the crossflow instability turns progressively to a first mode. N-factors at transition are around five.

Nomenclature

A = amplitude of a perturbation
A_0 = initial amplitude of a perturbation
a = speed of sound, m/s
f = frequency, s^{-1}
H = enthalpy, J/kg
M = Mach number
P = pressure, Pa
PP = average of the pitot pressure measured over the front cross section of the pitot probe
Re = Reynolds number
s = curvilinear abscissa, m
s_0 = neutral curve abscissa, m
T = temperature, K
U, V, W = mean flow velocity components along x, y, and z, m/s
$\mathbf{V_g}$ = group velocity vector, m/s
X, Y, Z = coordinates in the global reference frame attached to the vehicle, m
x, y, z = streamwise, normal-to-the-wall, and spanwise coordinates, m
α, β = wave numbers (complex) in the x and z directions, m^{-1}
δ = boundary-layer thickness, m
δ_* = displacement thickness, m
ϵ = boundary-layer edge parameter
θ_g = direction of $\mathbf{V_g}$
μ = viscosity, kg/m · s
ρ = density, kg/m^3
ψ = wave propagation angle
$\bar{\psi}$ = wave amplification angle
ω = $2\pi f$, pulsation, s^{-1}

Subscripts

dyn = dynamic value (pressure)
M = maximum value
stat = static value
tot = total (or stagnation) value
u = unit length
w = value at the wall
∞ = static value at infinity

Superscript

e = value in the freestream, outside the boundary layer

I. Introduction

THE prediction of laminar–turbulent transition in wall-bounded flows is mandatory in the design process of hypersonic airbreathing vehicles. Transition has important consequences on surface heating, skin friction, and other boundary-layer (BL) properties, like separation [1]. Indeed, a turbulent BL coming in to the air inlet of a scramjet engine is more likely to withstand the pressure gradients without separation. However, the transition prediction is still a challenging task after half a century of intensive research, both experimental and computational. Today, the most predictive computational methods of industrial application are based on the linear stability theory (LST, normal modes analysis) and rely on the semi-empirical e^N method [2,3]. The key parameter is the value of the N-factor at transition, which must be empirically determined for a particular environment, either quiet (flight conditions, quiet wind tunnels) or noisy (conventional wind tunnels) [4]. A recent successful comparison between stability calculations and experiments has been done in the context of the Hypersonic International Flight Research Experimentation flight-test program [5,6].

The natural transition under flight conditions has been investigated numerically in a previous study [7], at Institut de Combustion Aérothermique, Réactivité, et Environnement–Centre National de la Recherche Scientifique for the flow under the full-scale three-dimensional hypersonic forebody shown in Fig. 1. The effects of Mach number (denoted as $\mathrm{M}_\infty = 4$, 6, and 8), angle of attack (denoted as AoA = 2, 4, and 6 deg), freestream dynamic pressure ($P_{\mathrm{dyn}} = 20$ and 60 kPa) through flight altitude, and wall thermal conditions have been investigated. The aim of this paper is 1) to

---

Presented as Paper 2009-7352 at the 16th AIAA/DLR/DGLR International Space Planes and Hypersonic Systems and Technologies Conference, Bremen, Germany, 19–22 October 2009; received 13 July 2010; revision received 10 February 2011; accepted for publication 10 February 2011.

*Ph.D. Student, Institut de Combustion Aérothermique, Réactivité, et Environnement, 1C Avenue de la Recherche Scientifique.

†Associate Professor, Institut de Combustion Aérothermique, Réactivité, et Environnement, 1C Avenue de la Recherche Scientifique. Member AIAA.

‡Senior Research Associate, Institut de Combustion Aérothermique, Réactivité, et Environnement, 1C Avenue de la Recherche Scientifique. Member AIAA.

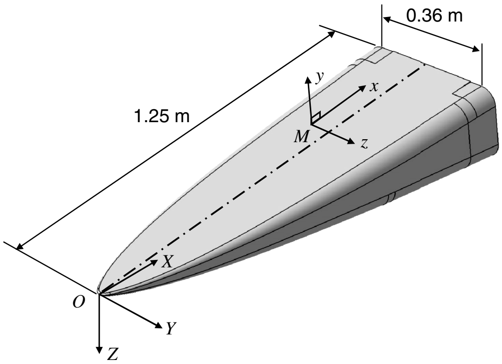

Fig. 1 CAD view of the forebody lying on its back, full scale; $\{X, Y, Z\}$ is the global reference for the vehicle, and $\{x, y, z = Y\}$ is the reference frame attached to the wall at a point M.

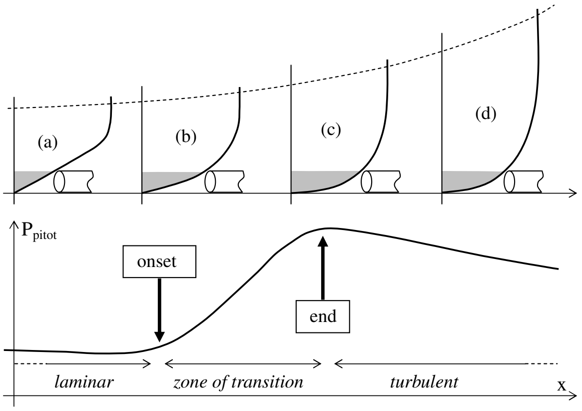

Fig. 3 Schematic illustrating the method used to detect the transition using a pitot tube: a) laminar, b) onset of transition, c) end of transition, and d) turbulent.

report the results of transition experiments at $M_\infty = 4$ and 6 on the 1:3-scale model shown in Fig. 2, in the T-313 conventional blowdown wind tunnel of the Institute of Theoretical and Applied Mechanics (ITAM)–Russian Academy of Science at Novosibirsk, and 2) to assess the predictive capabilities of the LST e^N method for these experiments. The model includes a compression ramp 478 mm downstream from the nose, not present on the full-scale CAD view, which is cut before the ramp.

This paper is organized as follows. Section II describes the experimental setup and the flow parameters. Global features of the flow are illustrated with schlieren and oil flow visualization. Transition results are given, deduced from pitot pressure measurements. Section III gives an overview of the numerical methodology, regarding both computational fluid dynamics (CFD) simulations and stability analysis. Additional insight from CFD, on the structure of the flow, and results from the stability analysis are provided. N-factors are computed and correlated with experimental transition points.

II. Experiments

A. Facilities and Instrumentation

The T-313 blowdown wind tunnel is fed from a huge air storage at 2 MPa, which allows continuous 5-min runs at a maximum total pressure of 1.2 MPa and a total temperature of 700 K. The Mach number ranges from 1.8 to 7, and the maximum unit Reynolds number is $60 \times 10^6\ \mathrm{m}^{-1}$. Because the flow regime is continuous and the total temperature in the present experiments is close to room temperature, the wall of the model, which initially is at room temperature, is able to reach thermal equilibrium during a run. Hence, usual transition detection by heat transfer measurements is not possible [8]. Transition is indicated by the change in pitot pressure in the BL, due to the change in the shape of velocity profiles or in the displacement thickness along the transition zone: a turbulent BL profile is more “filled” than a laminar one, hence, producing a higher pitot pressure. By moving a pitot tube, lying on the wall downstream, the onset of transition is associated with an increase in the measured pressure. This pressure, hereafter designated as *PP*, is the average of the pitot pressure at the front cross section of the pitot tube. At the end of transition, the PP is at its maximum value. Then, due to turbulent diffusion, the BL thickness increases and the PP decreases. Figure 3 illustrates the principle of the method, which has been successfully applied by V. Kornilov, from ITAM, in flat-plate experiments in T-313 [9].

Two rakes with three pitot tubes have been designed for $M_\infty = 4$ and 6, allowing for three spanwise simultaneous measurements. The tips of the tubes have been, respectively, flattened to 0.1 and 0.2 mm, in order to stay below 20% of the predicted laminar BL thickness. In the early development of the BL near the nose, this requirement is not perfectly fulfilled, but this size of the probes has proven to give the highest PP variation across the transition zone in the experiments of [9]. Pressure transducers are Siemens KPY 4x-A Infineon Technologies silicone piezoresistive absolute pressure sensors.

Because at $M_\infty = 4$ the transition is expected near the nose of the forebody, the pitot tubes are set closer to each other than those designed for the runs at $M_\infty = 6$, in which transition is rather expected in the wider middle part of the body. The spanwise locations have been chosen to cover the forebody width, but to stay within the compression ramp width. Each of the pitot tubes is connected to an independent electrical circuit. The rake is moved downwards until one of the tubes contacts the wall. The rake can then be moved along the body with an axial amplitude of 200 mm. At a given position, the rake can also be moved normal to the wall to measure the PP profile. Figure 4 shows the installation of the forebody in the test section of T-313, for pitot rake measurements. During some runs, schlieren visualizations of the structure of the flow have also been done. Moreover, some runs have been dedicated to oil flow visualization of the wall friction lines, to demonstrate crossflow (CF) presence. In this

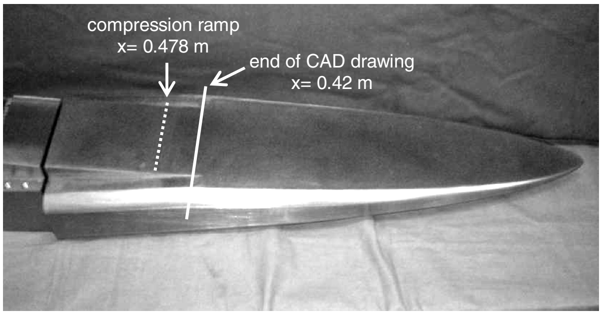

Fig. 2 1:3-scale model of the forebody for transition experiments, including a compression ramp.

Fig. 4 Model in the test section of T-313 for pitot rake measurements.

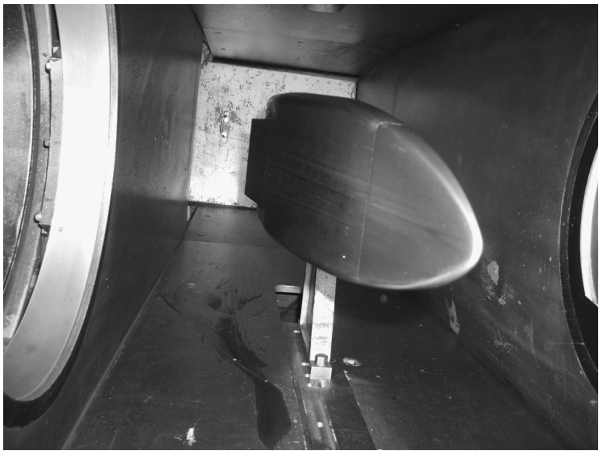

Fig. 5 Setup of the model for oil flow visualizations.

case, the model is installed differently in the test section, in front of the optical access (Fig. 5).

B. Flow Parameters and Visualizations

In all the experiments, the angle of attack is 4°. The leeward surface of the forebody is almost parallel to the freestream, and the windward surface, of interest for the BL investigation, is inclined 8° to the flow direction. Nominal parameters are given in Table 1.

The computed static temperature and pressure are 67 K and 6815 Pa at $M_\infty = 4$, and 46 K and 543 Pa at $M_\infty = 6$. Because the pressure is low, nitrogen does not liquefy at these very low temperatures. During a run, the total parameters of the flow are sampled from time to time by the operator. They vary slightly, as shown in Fig. 6. The deviation is about 1% at $M_\infty = 4$ and about 3% at $M_\infty = 6$. Hence, all the results presented hereafter concerning the PP are normalized with the instantaneous total pressure.

Figure 7 shows a nice visualization of the leading shock at $M_\infty = 4$ (run 1). Figure 8 is an image of the pitot rake in run 2, $M_\infty = 6$. The lighter near-wall region corresponds to the BL where the temperature is higher, yielding lower near-wall densities.

An oil flow visualization of the wall friction lines is given in Fig. 9 (run 5, $M_\infty = 4$). It shows the presence of CF from the attachment line near the nose leading edge, toward the plane of symmetry. CF occurs because the shock is closer to the lateral edge than to the upper and lower walls (the shock has a quasi-elliptic cross section, which surrounds the quasi-rectangular cross section of the body). Hence, a pressure gradient drives the near-wall flow toward the centerline of the forebody. This phenomenon is the same as the one observed by Kimmel et al. [10,11] on an elliptic cone. The higher the Mach number, the more CF is observed, because the shock wave is more oblique and lies closer to the body.

C. Transition Results

All of the results are presented in the coordinate system $\{x, y, z\}$, attached to the wall (Fig. 1). The origin of the z axis is at the symmetry plane, and the y axis is normal to the wall. Because the wall is a plane, this coordinate system is the same for the whole surface. The PP distribution has been measured and computed along the lines drawn in Fig. 10, and profiles have been measured and computed at the ends of the lines. Details of computations are given in Sec. III.A.

Table 1 Nominal flow parameters for experiments in the T-313 wind tunnel

Run number	M_∞	P_{tot}, MPa	T_{tot}, K	Re_u, m^{-1}	Visualization
1	4	1.03	283	49.4×10^6	Schlieren
2	6	0.85	380	10.9×10^6	Schlieren
3	6	0.82	380	10.5×10^6	Schlieren
4	6	0.80	320	13.9×10^6	Oil flow
5	4	1.00	283	48.0×10^6	Oil flow

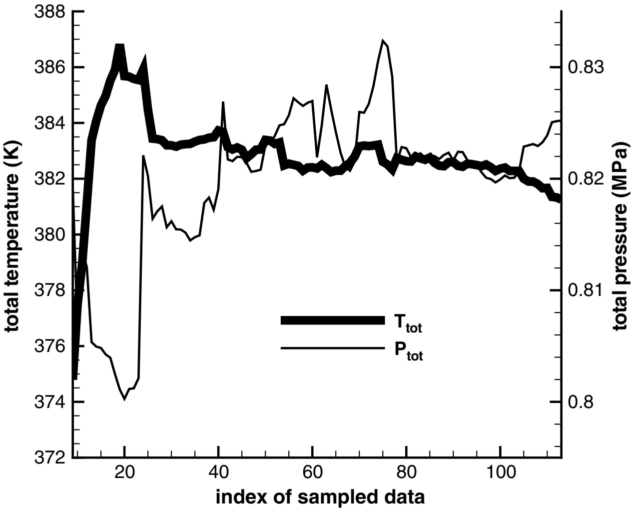

Fig. 6 Variations of total temperature and pressure during run 3, $M_\infty = 6$.

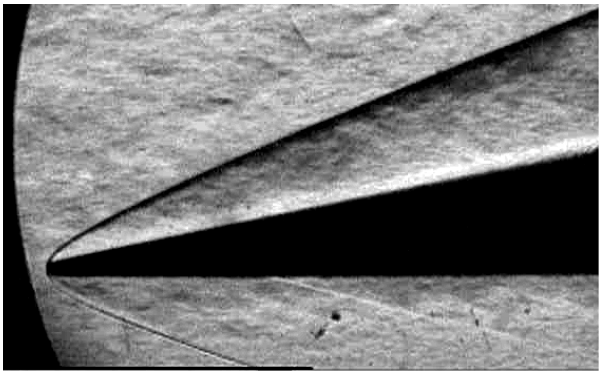

Fig. 7 Schlieren visualization, run 1, $M_\infty = 4$.

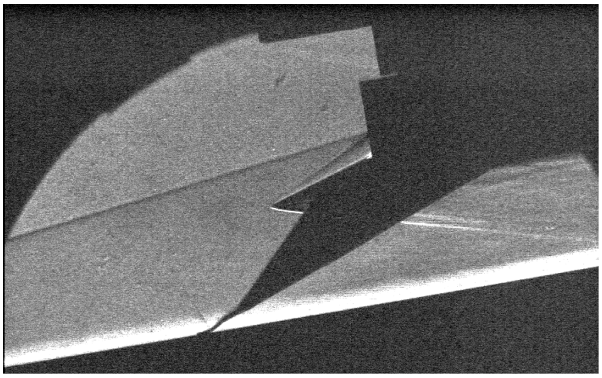

Fig. 8 Schlieren visualization, run 2, $M_\infty = 6$, showing the pitot tubes in the BL and the support of the rake (obstruction).

The computations for a turbulent flow do not claim to be predictive, but have been done for a qualitative comparison with experimental results.

Run 1: $M_\infty = 4$. Figure 11 shows the evolution of the measured and computed PP along the lines with corresponding symbols. One can clearly see an increase in PP up to a maximum, followed by a decrease typical of a turbulent BL. The computed PP for a turbulent flow qualitatively confirms the trend. Since a laminar calculation does not correlate with the experimental data, transition has occurred. This is confirmed by the PP profiles measured at $x = 25$ mm (Fig. 12) and $x = 205$ mm (Fig. 13). At $x = 25$ mm, PP profiles are

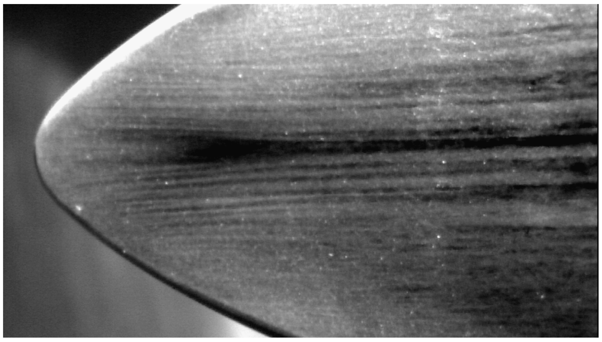

Fig. 9 Oil flow visualization: wall friction lines show CF toward the plane of symmetry, run 5, $M_\infty = 4$.

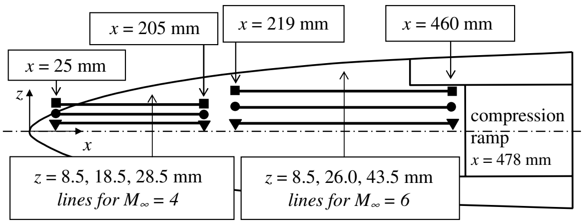

Fig. 10 Lines of measurement along x for the PP distribution of Figs. 11 and 14 and location of PP profiles of Figs. 12 and 13 (run 1, $M_\infty = 4$) and Figs. 16 and 17 (runs 2 and 3, $M_\infty = 6$).

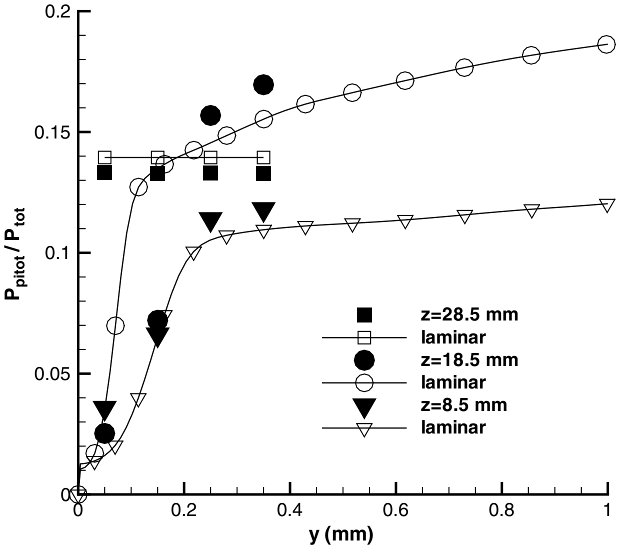

Fig. 12 Measured (filled symbols) and computed PP profiles, $x = 25$ mm: run 1, $M_\infty = 4$.

close to those of a laminar BL. At this abscissa, it is clear that the 0.1 mm probe height exceeds 50% of the BL thickness and is above the sonic line. Hence, measured PPs are quite different from local pitot pressures. The laminar character of the flow is obvious. One can also notice that the outermost tube (square symbols, $z = 28.5$ mm) touches the wall for $x \gtrsim 50$ mm. Hence, at $x = 25$ mm, this tube is outside the shock, and the measured profile is that of the freestream at $M_\infty = 4.05$. At $x = 205$ mm, Fig. 13 shows that the measured PP profiles are more similar to those of a turbulent BL than to those of a laminar one. Moreover, for the tube at $z = 8.5$ mm location, computed data closely agree with measured PP profiles.

So, at $M_\infty = 4$, for the conditions of run 1, transition occurs very close to the nose, although the transition onset points are not obvious in Fig. 11. They can be estimated at $x = 25$ mm, where the first profiles have been measured. According to the peaks of PP observed in the figure, one can estimate the end of transition at $x \approx 50$ mm for $z = 8.5$ mm, at $x \approx 35$ mm for $z = 18.5$ mm, and at $x \approx 60$ mm for $z = 28.5$ mm.

Runs 2 and 3: $M_\infty = 6$. The unit Reynolds number is much lower than for run 1 (see Table 1), and the Mach number is higher. Hence, transition is expected to move downstream toward the middle of the forebody. The model is placed in the test section, so that measurements begin at $x = 219$ mm. Figure 14 shows the PP measured along the lines identified in Fig. 10, and Fig. 15 is a zoom on the data at $z = 8.5$ mm. The probe lies everywhere below the computed sonic line, for a laminar as well as for a turbulent BL.

During run 2, the PP measured by the two outermost probes always increases (except a peak located at $x \approx 320$ mm and $z =$ 43.5 mm). This suggests that the beginning of transition is just at or immediately after $x = 219$ mm for $z = 26$ and 43.5 mm. The probe at $z = 8.5$ mm clearly indicates the onset point of transition at $x \approx 320$ mm in Fig. 15. Obviously, the end of transition is not reached during run 2 for any of the probes. For this reason, run 3 has been done with the model displaced by 100 mm upstream. This also allows us to test the repeatability of the measurements.

The 50 mm shift between the curves of run 2 and run 3, for the tubes located at $z = 26$ and 43.5 mm in Fig. 14, may have two

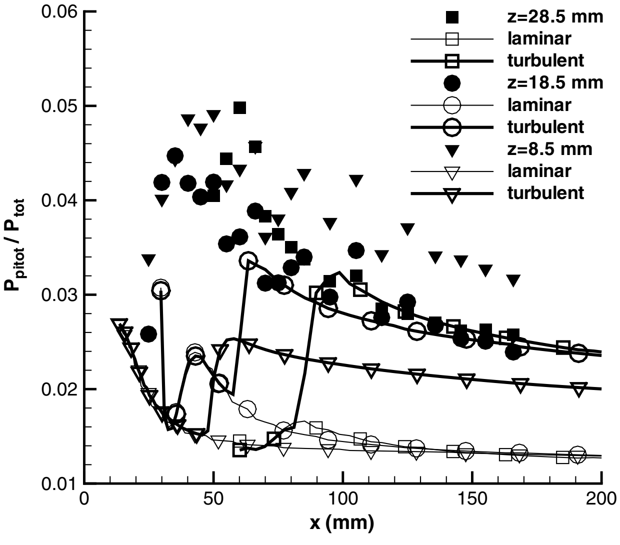

Fig. 11 Measured (filled symbols) and computed PP along the lines shown in Fig. 10: run 1, $M_\infty = 4$.

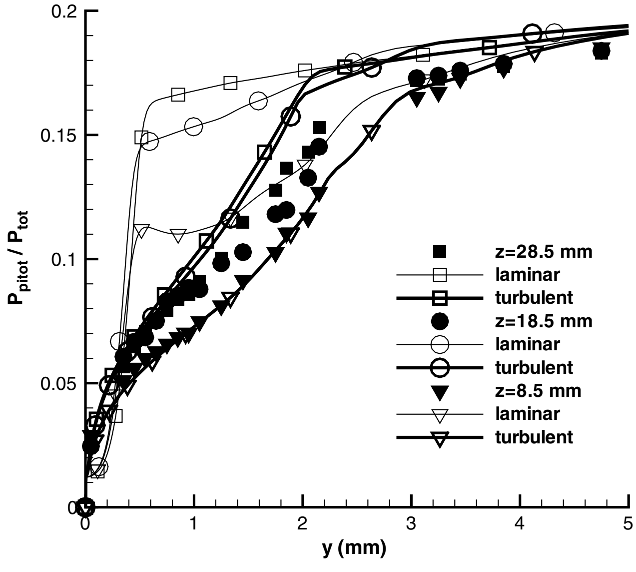

Fig. 13 Measured (filled symbols) and computed PP profiles, $x = 205$ mm: run 1, $M_\infty = 4$.

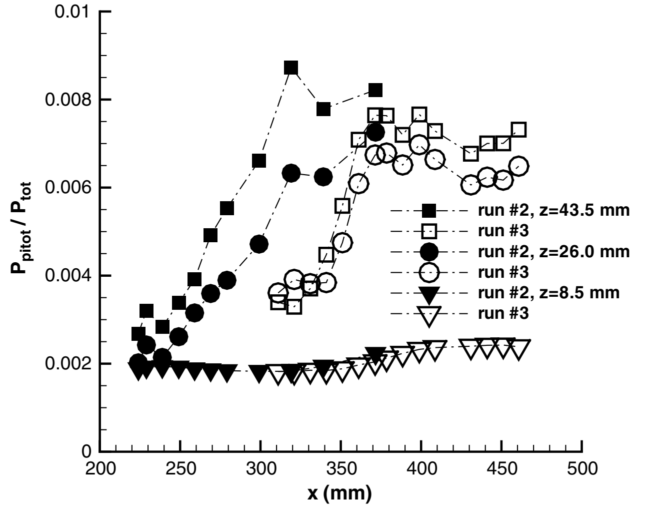

Fig. 14 Measured PP during run 2 (filled symbols) and run 3 (open symbols), along the lines shown in Fig. 10: $M_\infty = 6$.

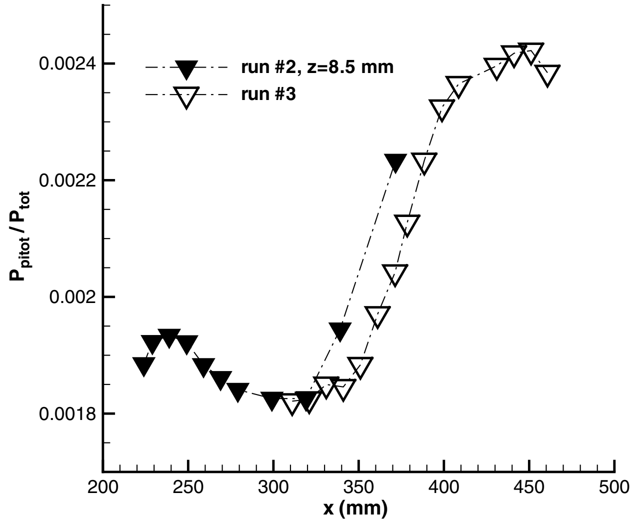

Fig. 15 Zoom on the data for $z = 8.5$ mm in Fig. 14.

probable causes: the unit Reynolds number has changed from 10.9×10^6 to 10.5×10^6 m^{-1}, delaying the beginning of the transition; and, because the mechanical displacement device visible in Fig. 4 is not absolutely rigid, the position of the rake has probably been controlled by the tube at $z = 8.5$ mm, for which the shift is smaller in Fig. 15. The other tubes may have been at slightly different altitudes during the two runs. It is recalled that the rake is moved downwards, until one of the tubes comes into electrical contact with the wall while the flow at $M_\infty = 6$ is running.

The PP profiles measured at $x = 219$ mm are very similar to those of laminar calculations (Fig. 16). Although the results for $z = 8.5$ mm are not as good as for $M_\infty = 4$, the zoom of the near-wall region rather indicates a laminar behavior. This confirms the results of Fig. 14, which show that this location is the very beginning of the transition. The profiles of Fig. 17, measured just before the compression ramp of the air inlet, are typical of a turbulent BL. Calculations have not been done at this location, the CAD model being cut before at $x = 430$ mm.

So, at $M_\infty = 6$, for the conditions of run 2, transition onset occurs at $x \approx 220$ mm for the probes at $z = 26$ and 43.5 mm and at $x \approx 320$ mm for the probe at $z = 8.5$ mm, close to the plane of symmetry. During run 3, the end of transition is observed, respectively, at $x \approx 400$ mm for the two former probes and $x \approx 450$ mm for the latter.

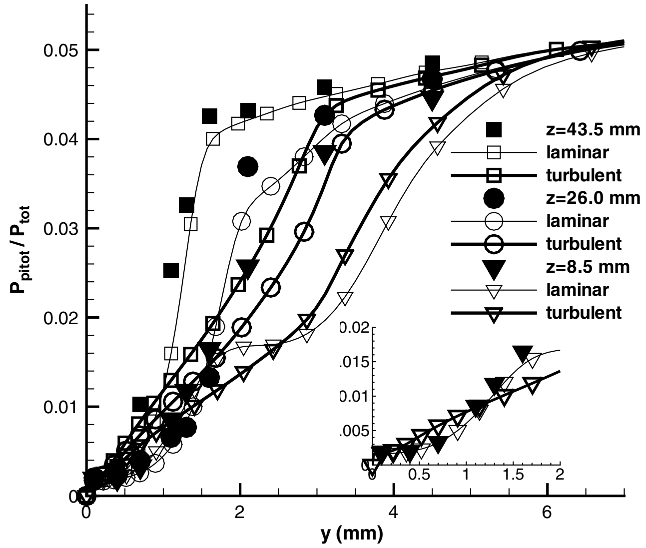

Fig. 16 Measured (filled symbols) and computed PP profiles, $x = 219$ mm, run 2, $M_\infty = 6$.

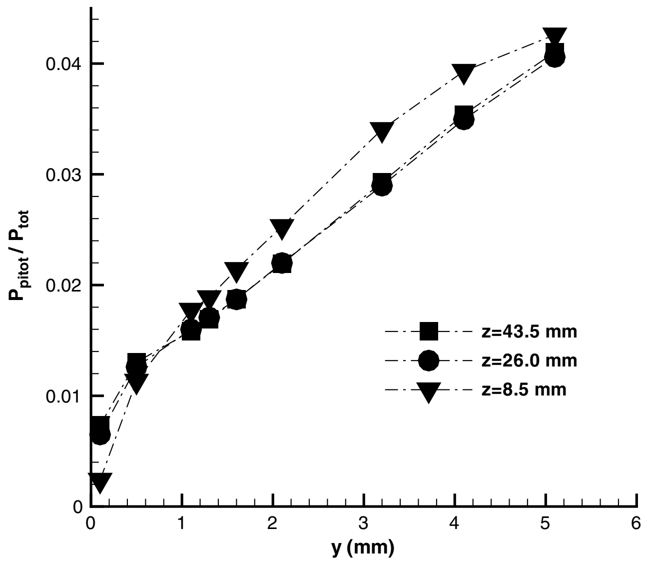

Fig. 17 Measured PP profiles, $x = 460$ mm, run 3, $M_\infty = 6$.

III. Computations

CFD and stability calculations have been performed for flight conditions and for the T-313 wind-tunnel conditions. In the simulations of experiments, the wall of the body is supposed adiabatic, as discussed in Sec. II.A. In flight conditions, the wall is radiating with high emissivity and is assumed to be in thermal equilibrium with the flow. Details about physical models (thermodynamics and transport), numerics, and validation of the method can be found in Ferrier et al. [7]. For conciseness, only the main features of the calculations are given here, emphasis being given to the results. In fact, calculations have been done before the experiments, for estimated values of the experimental conditions. Parameters of calculations are gathered in Table 2, to be compared with Table 1.

Table 2 Parameters of calculations to simulate experimental runs

Run	M_∞	P_{tot}, MPa	T_{tot}, K	P_{stat}, Pa	T_{stat}, K	Re_u, m^{-1}
1	4	0.98	283	6484	67.3	46.9×10^6
2–3	6	0.808	400	516	48.7	9.5×10^6

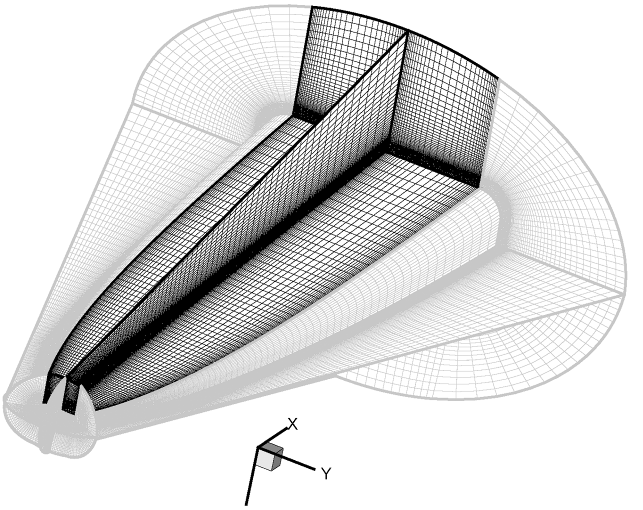

Fig. 18 Overview of the computational mesh; ZI is dark.

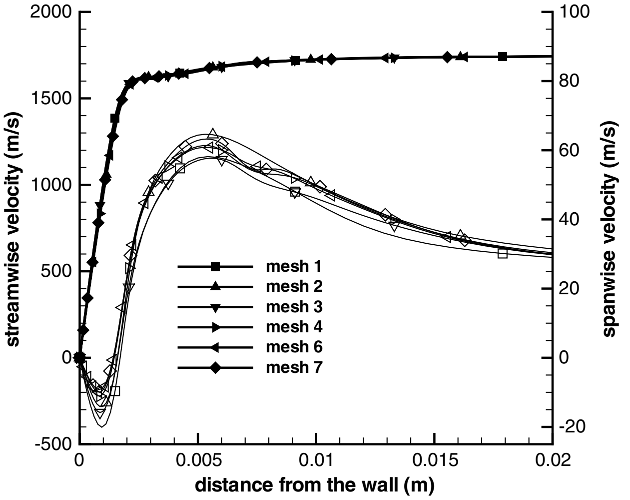

Fig. 19 Grid convergence: streamwise (filled symbols) and spanwise (open symbols) velocity components at $X = 0.5$ m and $Y = 0.05$ m, flight conditions, $M_\infty = 6$.

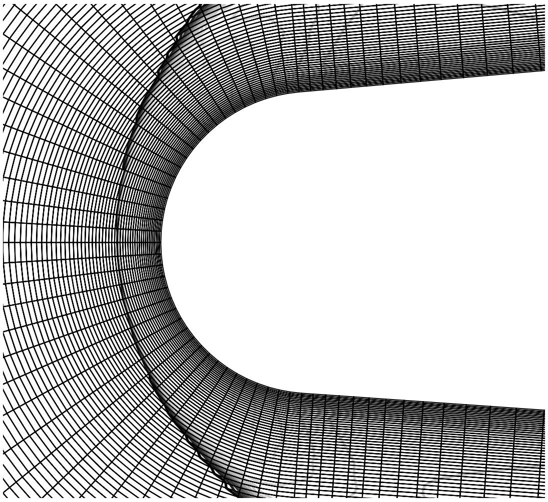

Fig. 20 Resolution of the shock at the nose, $M_\infty = 6$, full scale, mesh 4.

A. Computational Fluid Dynamics: Mean Flow

Calculations have been performed using the second-order upwind implicit density-based solver available in Fluent 6.3.26, with the Roe flux. The compressible Navier–Stokes equations, with fully variable thermodynamic and transport models, are solved. The objectives are threefold: 1) to obtain global information on the BL in the laminar and turbulent cases, like thicknesses, wall friction, recovery temperature, pitot pressure, etc. (these data are useful to design, for example, the pitot probes); 2) to obtain numerically the PP profiles in the laminar and turbulent cases for a comparison, at least qualitative, with the experimental profiles and, hence, to confirm the occurrence (or not) of transition; and 3) to obtain an accurate laminar mean flow for stability calculations. Figure 18 shows the computational mesh of the forebody lying on its back, to make visible the zone of interest (ZI, in dark in the figure) for the stability calculations. In this area, which starts 4 cm (full scale) from the nose, the wall is a plane in which the BL develops. Near the nose and on the edges of the body, the parallel flow assumption is not valid, and the local modal stability theory does not apply. In the nose region, the mesh is hexahedral and unstructured, and in the ZI the mesh is fully structured.

Turbulent calculations have used the Menter k-ω shear stress transport turbulence model [12]. The model is turned off in the nose region, to avoid an erroneous excessive production of turbulent kinetic energy across the shock. It is turned on quite arbitrarily in the ZI. This explains the transitional behavior of the computed PP in Fig. 11.

The grid convergence has been investigated by building different meshes, for which the parameters are gathered in Table 3. Meshes 1–4 and 6–7 are designed for $M_\infty = 6$ (and $M_\infty = 8$, flight conditions). Mesh 5 is for $M_\infty = 4$. In this case, the size of the computational domain is increased to avoid numerical reflection of the shock on external boundaries. For each mesh, the height of the first cell above the wall is less than 0.015 mm all along the body. The cell Reynolds number

$$Re_{\text{cell}} = \frac{\rho_w a_w \Delta y_w}{\mu_w} \tag{1}$$

is around 12–14 for $M_\infty = 4$ and around 2–4 for $M_\infty = 6$. The values for $M_\infty = 4$ are a little higher than recommended by Papadodouplos et al. [13] for an accurate wall heat flux prediction, but are sufficient for an adiabatic wall.

Table 3 Number of cells for the different meshes

Mesh number	ZI: X	ZI: Y	ZI: Z	Total, $\times 10^6$
1	56	32	71	0.9
2	90	32	101	1.7
3	90	40	101	2.0
4	90	60	101	2.0
5	95	72	141	3.3
6	90	60	201	4.5
7	90	60	201	5.1

Meshes 6 and 7 have been designed for a better resolution of the BL and of the nose region, compared with meshes 1–4. In mesh 7, the grading of the cells normal to the wall has been increased, compared with mesh 6, for an even finer resolution of the BL. Figure 19 shows the grid convergence for streamwise and spanwise velocity profiles located at $X = 0.5$ m and $Y = 0.05$ m, for the full-scale forebody in flight conditions at $M_\infty = 6$. There is no significant difference between the results of mesh 4 and those of meshes 6 and 7. So, for the simulation of runs 2 and 3 at $M_\infty = 6$, mesh 4 was retained.

Figure 20 shows the resolution of the shock at the nose in the plane of symmetry. In Fig. 19, the spanwise velocity component is associated with the CF pattern observed in Fig. 9 and has highly inflexional instability. Near the plane of symmetry, the flow rolls up into a pair of long longitudinal counter-rotating vortices, which are very difficult to destabilize. In this central part of the body, the entropy layer generated by the curved bow shock at the nose is swallowed downstream by the BL. This has been identified as a stable region, by Stetson et al. [14], on a blunt cone at $M_\infty = 8$. The stability results presented hereafter confirm this behavior.

Figure 21 shows the streamwise velocity and temperature profiles at $x = 0.2$ m for different spanwise locations. Calculations are done

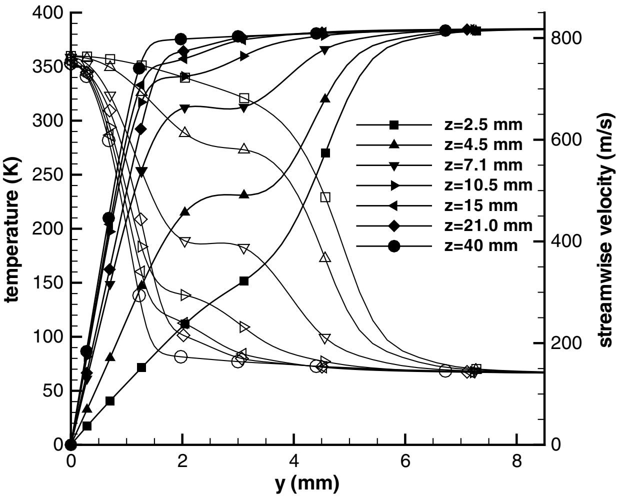

Fig. 21 Streamwise velocity (filled symbols) and temperature profiles (open symbols) at $x = 0.2$ m for different spanwise locations, $M_\infty = 6$, experimental conditions, mesh 4; symbols are every 10 grid points.

for the experimental conditions of runs 2 and 3. Symbols are plotted at every ten grid points. For the most central locations, $z = 2.5$, 4.5 and 7.1 mm, the profiles result from the combination of the longitudinal vortices and the entropy layer. From $z = 10.5$ to 21 mm, profiles are characteristic of a mixed boundary–entropy layer. At $z = 40$ mm, the entropy layer disappears, and standard BL profiles are obtained.

The definition of the edge of the BL is not obvious and is subject to discussion [15]. Starting in the freestream, the edge of the BL is found along a normal to the wall when the total enthalpy variation is greater than a prescribed value between two successive mesh points:

$$\delta\colon \left|\frac{H_{\text{tot}}(y_j) - H_{\text{tot}}(y_{j+1})}{H_{\text{tot}}(y_j)}\right| < \epsilon \tag{2}$$

This method differs slightly from the one proposed by Kimmel et al. [10], which defines the edge of the BL as the point at which the total enthalpy is 1.005 times the free-flow stagnation value. We found that this method gives too small values of δ. In Table 4, the results of the present method for different values of ϵ are compared with those of the Kimmel et al. criterion for some profiles of Fig. 21. Visually, the best estimation is obtained for $\epsilon = 5 \times 10^{-4}$. The laminar BL thickness is compared in Fig. 22 for runs 1 and 2. The BL thickness increases continuously from the nose to the end of the forebody, and is almost everywhere greater than the cross-sectional size of the pitot tubes described in Sec. II.A (0.1 mm for $M_\infty = 4$ and 0.2 mm for $M_\infty = 6$), used for the PP measurements presented in Sec. II.C.

To better understand the stability properties of the near-wall flow, the computed wall friction lines for $M_\infty = 4$ and $M_\infty = 6$ are displayed in Fig. 23 in the nose region and can be compared with the oil flow visualization (Fig. 9). At $M_\infty = 4$, one can see the attachment line close to the edge of the ZI, although it is not clearly visible in Fig. 9. At $M_\infty = 6$, the attachment line is moved outside of the ZI, on the lateral edge of the forebody (see Fig. 6 in [7]). Crossing the attachment line changes the sign of the CF velocity component. Some elements of the classical theory for the stability of attachment lines on swept wings can be found in [16].

Table 4 BL thickness (mm) for different criteria

ϵ in Eq. (2)	10^{-4}	5×10^{-4}	10^{-3}	10^{-2}	Kimmel et al. [10]
$z = 2.5$ mm	7.28	5.95	5.96	5.42	5.68
$z = 7.1$ mm	6.55	5.17	4.95	1.48	4.74
$z = 15$ mm	3.47	3.34	1.77	1.54	1.69
$z = 40$ mm	4.09	1.80	1.72	1.57	1.65

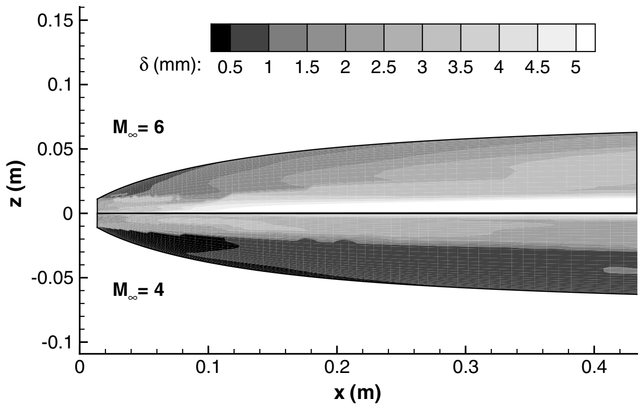

Fig. 22 Laminar BL thickness computed for run 1 ($M_\infty = 4$) and run 2 ($M_\infty = 6$), Eq. (2), $\epsilon = 510^{-4}$.

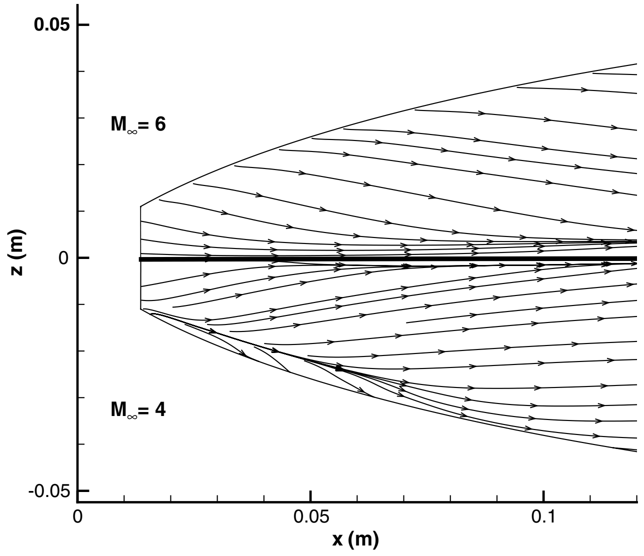

Fig. 23 Wall friction lines for $M_\infty = 6$ (top) and $M_\infty = 4$ (bottom) in the nose region.

B. Stability Analysis

The well-known modal local LST, in a fully compressible formulation with variable thermodynamic and transport properties, is applied to the three-dimensional mean flow profiles obtained from laminar CFD simulations. The method has been validated on the $M_\infty = 10$ flat-plate case of Malik and Anderson [17]. In the coordinate system $\{x, y, z\}$, attached to the wall, a three-dimensional perturbation q' of any of the laminar mean flow variables $\{\rho, U, V, W, P, T\}$ takes the form of a normal mode:

$$q'(x, y, z, t) = \hat{q}(y) \exp[i(\alpha x + \beta z - \omega t)] \tag{3}$$

in which, in the spatial approach $\alpha = \alpha_r + i\alpha_i$ and $\beta = \beta_r + i\beta_i$, are the complex wave numbers in, respectively, the longitudinal and transverse directions, and $\omega = 2\pi f$ is the real pulsation. The direction of propagation of the wave is $\psi = \tan^{-1}(\beta_r/\alpha_r)$, and the local amplification $\sqrt{\alpha_i^2 + \beta_i^2}$ is observed in the direction $\bar{\psi} = \tan^{-1}(\beta_i/\alpha_i)$, which is a priori unknown and for the determination of which several approaches have been proposed [18–20]. In the present study, the direction of amplification has been taken as the direction θ_g of the real part of the group velocity $\boldsymbol{V_g}$, at which the energy of a wave packet travels:

$$\Re\{\boldsymbol{V_g}\} = \frac{\partial\omega}{\partial\alpha_r}\boldsymbol{x} + \frac{\partial\omega}{\partial\beta_r}\boldsymbol{z}; \qquad \tan\theta_g = -\left(\frac{\partial\alpha_r}{\partial\beta_r}\right)_\omega \tag{4}$$

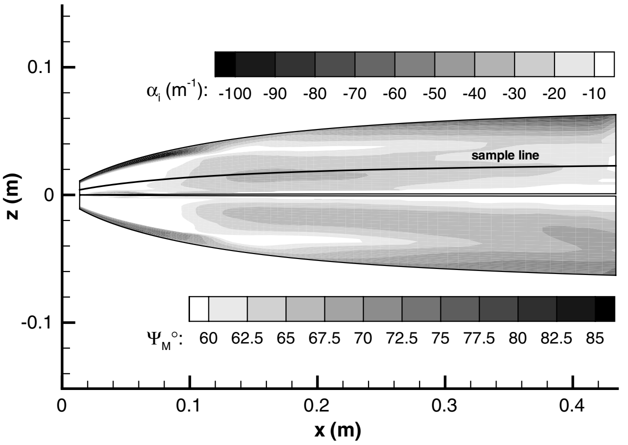

Fig. 24 First mode stability results: run 1, $M_\infty = 4, f = 30$ kHz.

An original method has been derived [7] to compute efficiently θ_g (but not $\Re\{\boldsymbol{V}_g\}$) in the spatial approach.

At each location, one seeks for a given frequency f the angle ψ_M giving the maximum amplification $\max_\psi \sqrt{\alpha_i^2 + \beta_i^2}$. This is the so-called envelope method. Then, the total amplification of a wave along an integration path tangent to the local group velocity direction θ_g is computed as

$$\frac{A}{A_0} = \exp\left\{\int_{s_0}^{s} \sqrt{\alpha_i^2 + \beta_i^2}|_{\psi=\psi_M}\,\mathrm{d}\xi\right\} = e^{N_f} \tag{5}$$

In Eq. (5), s_0 is the point on the integration path at which the wave with local amplitude A_0 becomes unstable. This gives the factor N_f for the considered frequency. The global N-factor is the envelope of N_f curves.

Stability results, run 1: $M_\infty = 4$. The LST indicates the coexistence of Mack's oblique first modes [or Tollmien–Schlichting-like (TS) waves] and CF instability. Between the edge of the ZI and the attachment line, TS and CF instabilities have ψ_M angles of the same sign, and between the attachment line and the symmetry plane, the angles are of opposite sign. The CF wavelengths are smaller (typically, $10 \sim 15\delta_*$) than those of the first modes ($20 \sim 50\delta_*$), as already observed in three-dimensional hypersonic flows [21]. Contour maps of α_i and ψ_M for TS waves over the ZI are provided in Fig. 24 for the frequency $f = 30$ kHz, which is roughly the most unstable one. Results along the sample mesh line drawn in Fig. 24 are given for frequencies $f = 10, 20, 30, 40,$ and 50 kHz. This line passes through the experimental onset of transition found with the tube located at $z = 8.5$ mm. Figures 25 and 26 show, respectively, the amplification rate α_i in the x direction and the angle of propagation ψ_M of the most unstable waves. Except outboard from the attachment line near the nose, this first mode instability is weak: the local amplification does not exceed -35 m^{-1}, and the waves are stable near the nose, inboard from the attachment line.

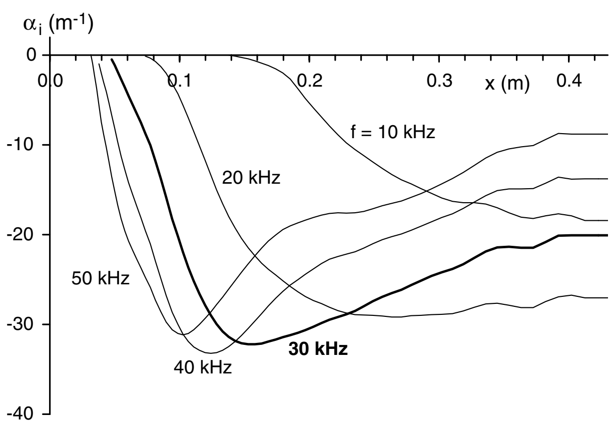

Fig. 25 Amplification rates α_i of the first mode along the sample line drawn in Fig. 22 for different frequencies, run 1, $M_\infty = 4$.

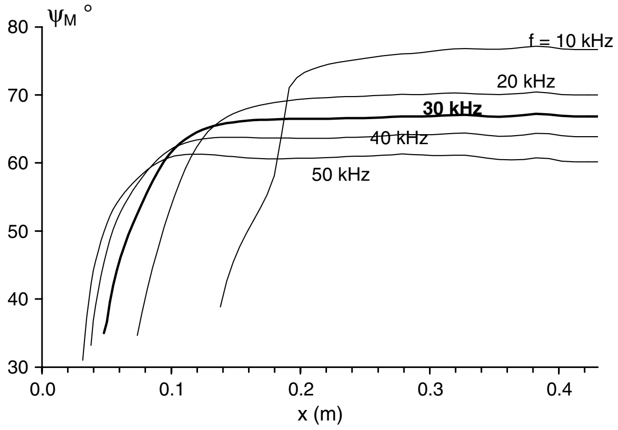

Fig. 26 Angle of propagation ψ_M of the first mode along the sample line drawn in Fig. 22, run 1, $M_\infty = 4$.

Contrary to the TS waves, the CF instability is very high, as seen in Fig. 27, which shows the contour maps of α_i and ψ_M for the CF wave of frequency $f = 30$ kHz. Amplification rates along the sample line are plotted in Fig. 28. They are as deep as -180 m^{-1} near the nose. Figure 29 shows the absolute value of the ψ_M angle, typical of CF waves near the nose. The angle decreases gradually downstream, to reach values which could be misinterpreted as those of a first mode instability. These CF waves have marginal instability at the end of the forebody. To distinguish between TS and CF waves, care must be

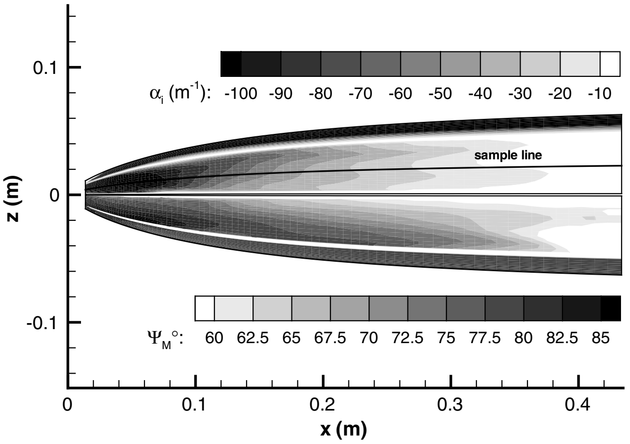

Fig. 27 CF stability results: run 1, $M_\infty = 4, f = 30$ kHz.

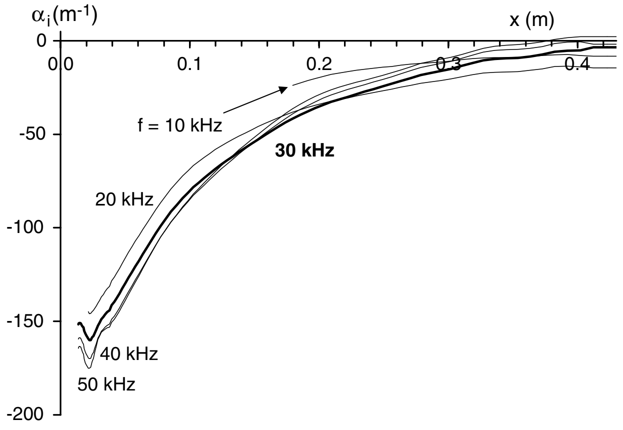

Fig. 28 Amplification rates α_i of CF instability along the sample line drawn in Fig. 27 for different frequencies, run 1, $M_\infty = 4$.

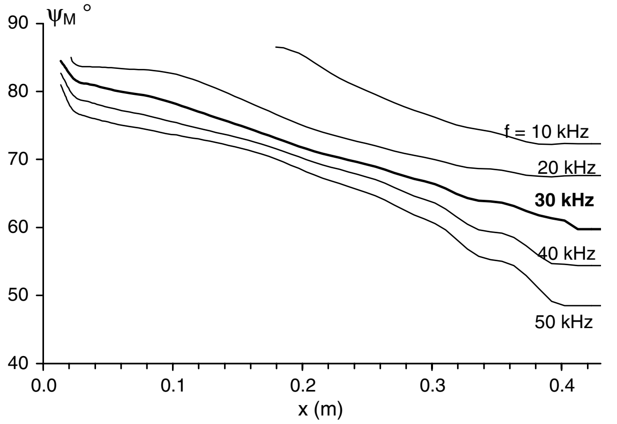

Fig. 29 Angle of propagation ψ_M (absolute value) of CF waves along the sample line drawn in Fig. 27, run 1, $M_\infty = 4$.

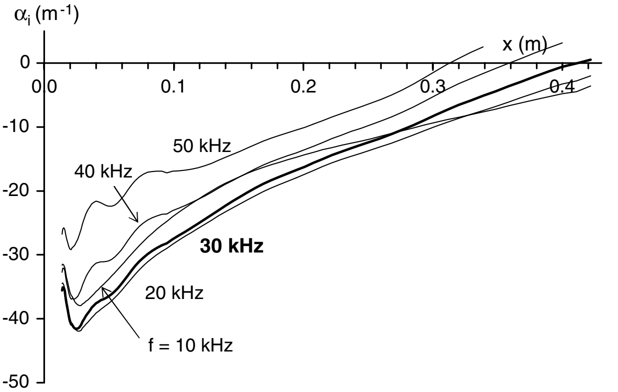

Fig. 31 Amplification rates α_i for line (a) in Fig. 30 for different frequencies, run 2, $M_\infty = 6$.

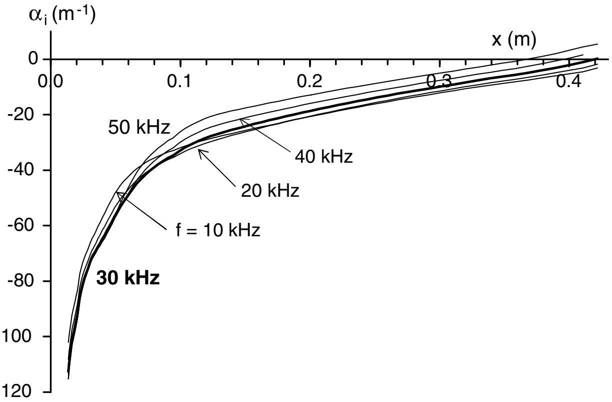

Fig. 32 Same as Fig. 31, line (b), run 2, $M_\infty = 6$.

taken to follow both instabilities, starting from the nose (where $|\psi_M|$ are clearly different) to the end of the forebody, making sure not to "jump" from one kind of wave to the other (i.e., checking the continuity of $\alpha_r(s)$).

A simple comparison between Figs. 24 and 27 leads to the conclusion that the experimental transition found close to the nose at $M_\infty = 4$, between the symmetry plane and the attachment line, is due to the CF instability, TS waves being stable at this location.

Stability results, runs 2 and 3: $M_\infty = 6$. Figure 30 shows the stability results for the frequency $f = 30$ kHz, which is again one of the most unstable, as shown in Figs. 31 and 32. These figures display the amplification rates along the specific mesh lines (a) and (b) of Fig. 30, which have been selected because they pass, respectively, through the experimental onset of transition found with the tubes located, respectively, at $z = 26$ and 43.5 mm. According to the very high ψ_M values observed near the nose in Figs. 33 and 34, the instability is clearly of the CF type, first. The ψ_M values progressively become typical of oblique first mode downstream. The amplification rate is lower than at $M_\infty = 4$, in accordance with the delayed transition observed in experiments during runs 2 and 3. A very weak instability (probably a first mode) has been detected, with a propagation angle of opposite sign, but it is so local and so weak that it plays little or no role in the transition process. Although the freestream Mach number is 6, the computed edge Mach number never exceeds 4.9, and no Mack's second mode instability [22] has been found.

C. *N*-Factor Results

In the semi-empirical e^N method, transition is supposed to occur for a prescribed value of N. In flight conditions, or for quiet wind tunnels, it is generally assumed that $N = 9 \sim 10$ are suitable values for transition due to first or second mode instabilities. In conventional wind-tunnel experiments, N-factor at transition depends on the environmental noise, which depends, in turn, on the Mach number, the unit Reynolds number, stagnation conditions, and many other parameters [22]. At high-noise level, N-factor at transition is usually $3 \sim 5$.

Little is known about N-factor at transition due to traveling CF disturbances in hypersonic flows. In the experiments of Cattafesta et al. [23], on a swept wing at Mach 3.5, $N = 13$ was found to correlate best with the observed transition location. During the Pegasus wing-glove flight experiment, Malik et al. [24] found transition N-factors between 7 and 12.3 for stationary disturbances ($f = 0$ Hz) and between 7.6 and 14.1 for traveling waves, the flight Mach number ranging from 4.13 to 4.99.

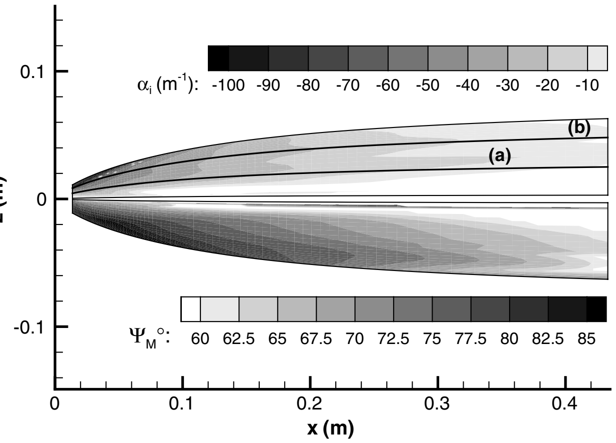

Fig. 30 Stability results, $f = 30$ kHz: run 2, $M_\infty = 6$.

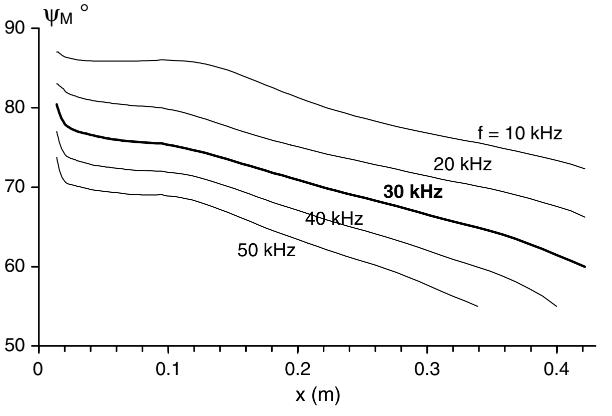

Fig. 33 Angle ψ_M of the most unstable waves for line (a) in Fig. 30, run 2, $M_\infty = 6$.

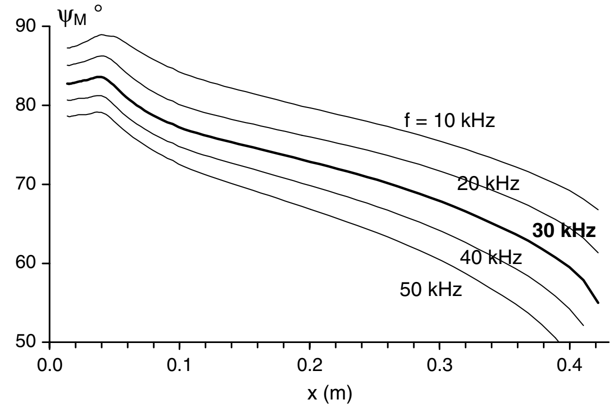

Fig. 34 Same as Fig. 33, line (b), run 2, $M_\infty = 6$.

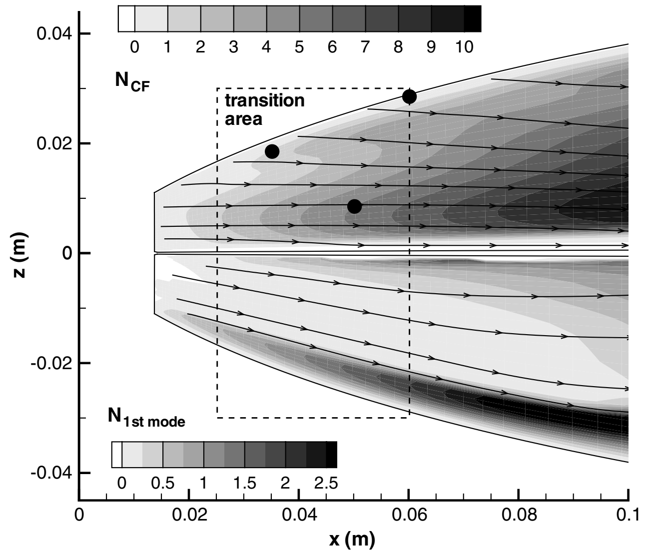

Fig. 35 Computed N-factors and experimental zone of transition: run 1, $M_\infty = 4, f = 30$ kHz; circles are the experimental end points of transition.

The integration of amplification rates, according to Eq. (5), starts at the edge of the ZI (see Fig. 18), not at the neutral curve. Hence, in the computation of N-factors with $N(s = 0)$ being set to zero, the total amplification of the area located between the neutral line and the beginning of the integration path on the edge of the ZI is not taken into account. It is difficult to accurately estimate the missing amount of amplification, but roughly, the ZI being 1.33 cm downstream from the nose, a constant $\alpha_i = -100\ \mathrm{m}^{-1}$ will generate an additional 1.33 value to the computed N-factor. In the case $M_\infty = 4$, Fig. 28 indicates rather $\alpha_i = -150\ \mathrm{m}^{-1}$; in the case $M_\infty = 6$, Fig. 32 indicates $\alpha_i = -120\ \mathrm{m}^{-1}$. So, the global uncertainty for the N-factors presented hereafter is less than two.

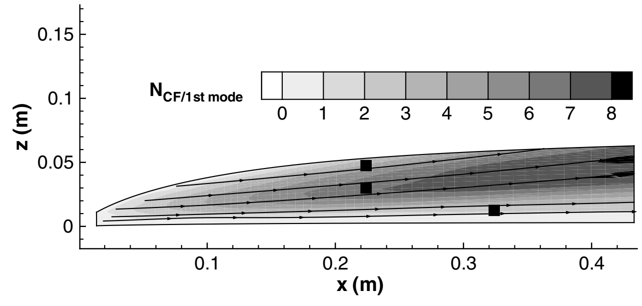

Fig. 36 Computed N-factors, runs 2 and 3, $M_\infty = 6, f = 30$ kHz; black squares are the experimental onset points of transition.

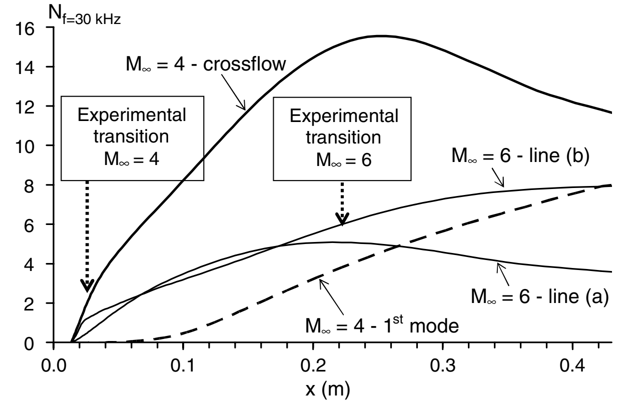

Fig. 37 Comparison of computed N-factors on the sample lines of Figs. 24 and 30, all runs, $M_\infty = 4$ and $6, f = 30$ kHz.

At $M_\infty = 4$, run 1, CF N-factors for $f = 30$ kHz reach a maximum value of 47 at the end of the forebody, whereas those of the first mode do not exceed 14. Figure 35 shows the map of the computed N-factors in the nose region, over which the experimental transition zone determined in Sec. II.C is depicted (dashed rectangle). The left border of the rectangle is at $x = 25$ mm, the estimated onset of transition from Fig. 11. The right border is at $x = 60$ mm, the transition end point for the outermost probe. The curves are the integration paths tangent to the group velocity. Transition starts where N-factors vary from 0.5 to 2, within the uncertainty previously mentioned. At $M_\infty = 6$, in the case of run 2, Fig. 36 shows that transition N-factors are around five. Finally, Fig. 37 compares N-factors on the selected sample lines for all runs.

IV. Conclusions

In this study, the laminar–turbulent transition on a hypersonic three-dimensional forebody has been investigated, both experimentally and numerically. It has been shown that a quite simple technique, based on PP measurements, can be used to detect the onset and end points of transition in a blowdown wind tunnel. This technique is, however, not suitable in an impulse wind tunnel, due to the short operation time. Transition occurs near the nose at Mach 4 and is delayed downstream at Mach 6. The modal LST, applied to mean flow profiles obtained from Navier–Stokes simulations, has allowed understanding, at least partially, of the instability mechanisms responsible for transition. It is concluded that transition is dominated by traveling CF disturbances of frequency around 30 kHz, which are very unstable on both sides of the attachment line at Mach 4, the attachment line itself being stable for traveling disturbances. At Mach 6, it was not possible to make a clear distinction between CF and first mode instability. Application of the empirical e^N method is not straightforward when three-dimensional geometries are considered, compared with flat-plate or cone flows. In the present study, the major cause of uncertainty is the lack of computed N-factor growth at the leading edge, between the neutral curve and the beginning of the integration path. This may be the subject for future investigation. However, within the uncertainty of the method, N-factors at the beginning of transition are around three for Mach 4 and around five for Mach 6.

Acknowledgments

We thank François Falempin from MBDA France, for financial support. We thank also M. Goldfeld from the Institute of Theoretical and Applied Mechanics, for hosting the experiments in the T-313 wind tunnel, and Jean Perraud from ONERA, for helpful discussions.

References

[1] Lau, K., "Hypersonic Boundary Layer Transition: Application to High Speed Vehicle Design," AIAA Paper 2007-310, Jan. 2007.

[2] Saric, W., Reshotko, E., and Arnal, D., “Hypersonic Laminar–Turbulent Transition,” AGARD Rept. 319, Vol. 2, 1998, pp. 2-1–2-27.

[3] Arnal, D., “Transition Prediction in Industrial Applications,” *Transition, Turbulence and Combustion Modeling*, edited by A. Hanifi, P. Alfredsson, A. Johansson, and D. Henningson, ERCOFTAC Series, Kluwer Academic, Norwell, MA, 1998, pp. 105–157.

[4] Schneider, S., “Effects of High-Speed Tunnel Noise on Laminar–Turbulent Transition,” *Journal of Spacecraft and Rockets*, Vol. 38, No. 3, 2001, pp. 323–333.
doi:10.2514/2.3705

[5] Whadams, T., Mundy, E., MacLean, M., and Holden, M., “Ground Test Studies of the HIFiRE-1 Transition Experiment Part 1: Experimental Results,” *Journal of Spacecraft and Rockets*, Vol. 45, No. 6, 2008, pp. 1134–1148.
doi:10.2514/1.38338

[6] Alba, C., Johnson, H., Bartkowicz, M., and Candler, G., “Boundary-Layer Stability Calculations for the HIFiRE-1 Transition Experiment,” *Journal of Spacecraft and Rockets*, Vol. 45, No. 6, 2008, pp. 1125–1133.
doi:10.2514/1.37445

[7] Ferrier, M., Fedioun, I., Orlik, E., and Davidenko, D., “Modal Linear Stability of the Near-Wall Flow on a Hypersonic Forebody,” *Journal of Spacecraft and Rockets*, Vol. 46, No. 1, 2009, pp. 51–66.
doi:10.2514/1.37093

[8] Orlik, E., “Etude du champ aérodynamique et de la transition laminaire–turbulent sur l’avant corps d’un véhicule hypersonique,” Ph.D. Dissertation, Univ. of Orléans, Orléans, France, 2009.

[9] Kornilov, V., “Transition of the Boundary Layer on a Flat Plate at Supersonic and Hypersonic Velocities,” *Thermophysics and Aeromechanics*, Vol. 16, No. 3, 2009, pp. 347–354.
doi:10.1134/S0869864309030032

[10] Kimmel, R., Klein, M., and Schwoerke, S., “Three-Dimensional Hypersonic Laminar Boundary-Layer Computations for Transition Experiment Designs,” *Journal of Spacecraft and Rockets*, Vol. 34, No. 4, 1997, pp. 409–415.
doi:10.2514/2.3236

[11] Kimmel, R., Poggie, J., and Schwoerke, S., “Laminar–Turbulent Transition in a Mach 8 Elliptic Cone Flow,” *AIAA Journal*, Vol. 37, No. 9, 1999, pp. 1080–1087.
doi:10.2514/2.836

[12] Menter, F., “Two-Equation Eddy-Viscosity Turbulence Models for Engineering Applications,” *AIAA Journal*, Vol. 32, No. 8, 1994, pp. 1598–1605.
doi:10.2514/3.12149

[13] Papadopoulos, P., Venkatapathy, E., Prabhu, D., Loomis, M., and Olynick, D., “Current Grid-Generation Strategies and Future Requirements in Hypersonic Vehicle Design, Analysis and Testing,” *Applied Mathematical Modelling*, Vol. 23, No. 9, 1999, pp. 705–735.
doi:10.1016/S0307-904X(99)00007-4

[14] Stetson, K., Thompson, E., Donaldson, J., and Siler, L., “Laminar Boundary Layer Stability Experiments on a Cone at Mach 8: Blunt Cone,” AIAA Paper 1984-0006, July 1984.

[15] Liechty, D., Berry, S., Hollis, B., and Horvath, T., “Comparison of Methods for Determining Boundary Layer Edge Conditions for Transition Correlations,” AIAA Paper 2003-3590, June 2003.

[16] Arnal, D., Perraud, J., and Séraudie, A., “Attachment Line and Surface Imperfection Problems,” *Advances in Laminar–Turbulent Transition Modelling*, 2009.

[17] Malik, M., and Anderson, E., “Real Gas Effects on Hypersonic Boundary-Layer Stability,” *Physics of Fluids A*, Vol. 3, No. 5, 1991, pp. 803–821.
doi:10.1063/1.858012

[18] Cebeci, T., and Stewartson, K., “On Stability and Transition in Three-Dimensional Flows,” *AIAA Journal*, Vol. 18, No. 4, 1980, pp. 398–405.
doi:10.2514/3.50772

[19] Nayfeh, A., “Stability of Three-Dimensional Boundary Layer,” *AIAA Journal*, Vol. 18, No. 4, 1980, pp. 406–416.
doi:10.2514/3.50773

[20] Mack, L., “Stability of Three-Dimensional Boundary Layers on Swept Wings at Transonic Speeds,” *IUTAM Symposium Transsonicum 3, Göttingen*, edited by J. Zierep and H. Oertel, Springer–Verlag, New York, 1988.

[21] Poggie, J., Kimmel, R., and Schwoerke, S., “Travelling Instability Waves in a Mach 8 Flow over an Elliptic Cone,” *AIAA Journal*, Vol. 38, No. 2, 2000, pp. 251–258.
doi:10.2514/2.979

[22] Mack, L., “Linear Stability Theory and the Problem of Supersonic Boundary-Layer Transition,” *AIAA Journal*, Vol. 13, No. 3, 1975, pp. 278–289.
doi:10.2514/3.49693

[23] Cattafesta, L., Iyer, V., Masad, J., King, R., and Dagenhart, J., “Three-Dimensional Boundary-Layer Transition on a Swept Wing at Mach 3.5,” *AIAA Journal*, Vol. 33, No. 11, 1995, pp. 2032–2037.
doi:10.2514/3.12944

[24] Malik, M., Li, F., and Choudhari, M., “Analysis of Crossflow Transition Flight Experiment Aboard the Pegasus Launch Vehicle,” AIAA Paper 2007-4487, June 2007.

R. Kimmel
Associate Editor